Dry-Type Phantom Emulating Quadrupole-Like Magnetic Field Distribution for Evaluation of Magnetoneurography

Yoshiaki Adachi (足立善昭)[1], Daisuke Oyama (小山大介)[1], Gen Uehara (上原弦)[1], and Shigenori Kawabata (川端茂徳)[2,3]

[1]Applied Electronics Laboratory, Kanazawa Institute of Technology, Kanazawa 920-1331, Japan
[2]Department of Advanced Technology in Medicine, Tokyo Medical and Dental University, Tokyo 113-8519, Japan
[3]Section of Orthopaedic and Spine Surgery, Graduate School of Tokyo Medical and Dental University, Tokyo 113-8519, Japan

This study proposes a dry-type phantom for evaluating the accuracy of magnetoneurography (MNG). The phantom emulates the quadrupole-like pattern of the typical magnetic field distribution observed in MNG. It is composed of a printed circuit board (PCB) patterned with long rectangular coils, whose short and long edges measure 5 and 360 mm, respectively. The magnetic field distribution from the dry-type phantom was obtained using a 132-ch MNG system equipped with an array of vector-type superconducting quantum interference device (SQUID) flux sensors, and it showed a clear quadrupole-like pattern. The dry-type phantom is easier to handle and provides comparable or higher accuracy than that of the previously developed wet-type phantom in terms of goodness of fit (GOF).

***Index Terms*— Biomagnetics, inverse problem, phantoms, superconducting quantum interference devices (SQUIDs).**

I. Introduction

MAGNETONEUROGRAPHY (MNG), a type of biomagnetic measurement, is a promising technique for non-invasive investigation of functioning of spinal cord and/or peripheral nerves [1], [2], [3], [4], [5]. The weak magnetic fields induced by the electrical activity of neurons are captured by an array of superconducting quantum interference device (SQUID) magnetic flux sensors arranged along the body surface. The current variation along the neurons accompanying the neural activity can be estimated from the obtained magnetic field distribution through appropriate magnetic source analyses [1], [2]. The neural signal propagation can be visualized as a transition of the estimated neural current along the spinal cord [2], [3] or peripheral nerves [4]. The lesions in the neurons are non-invasively localized with the decrease in the estimated current intensity and/or delay in the signal propagation at certain locations [2]. MNG provides significant diagnostic information about the rigorous localization of neural lesions, which is generally unavailable when the anatomical information is obtained through X-ray computed tomography or magnetic resonance imaging alone.

In biomagnetic measurements, phantoms that imitate neural activity using artificial currents are often used to evaluate the accuracy and spatial resolution of the current estimation. Several phantoms have been reported for evaluating magnetoencephalography (MEG). Phantoms are broadly classified as wet-type [6], [7] and dry-type phantoms [8]. Wet-type phantoms are composed of electrodes arranged in a vessel filled with saline water, which emulates both current dipoles and volume current to compensate for the current sources [9]. This is a typical model which emulates the current induced by the neural activities in the brain. However, it is difficult to position the electrodes accurately in the saline water, which often makes it difficult to discuss the uncertainties in the magnetic source analysis. The electric double layer around the electrodes also affects the current distribution in saline water [10].

The dry-type MEG phantom is based on the proposal by Ilmoniemi et al. [11] that an isosceles triangular coil with an infinitely small base will generate a magnetic field distribution exactly the same as that generated by an equivalent current dipole (ECD) in the conductive sphere formulated by Sarvas [12]. Compared to the wet-type phantom, it is significantly easier for a dry-type phantom to handle and achieve precise mechanical positioning of the electrodes, which makes it easier to calibrate the phantom.

Phantoms are effective in evaluating the accuracy of the MNG as well as the MEG. In our previous study, we proposed two wet-type phantoms for magnetospinography (MSG), which is a form of MNG, using the concept of wet-type MEG phantoms. The first emulation was a pair of ECDs of Sarvas's horizontally layered planar conductor model using catheter electrodes and a rectangular thin vessel filled with saline water [13]. The second was composed of a cylindrical vessel filled with saline water and a set of modeled vertebrae, which acted as a model of the neck [14]. They were effective in artificially realizing a quadrupole-like pattern, which was the magnetic field distribution typically observed in MSG or MNG. However, it had the same limitations in terms of accuracy as the wet-type MEG phantoms. Furthermore, it was difficult to obtain stable results from the wet-type MNG phantoms because it was difficult to maintain the surface of the saline water level. The conventional dry-type MEG phantoms cannot be applied to MNG because they assume a spherical conductor and do not fit to the spinal cord and/or peripheral nerves. In this study, we propose a dry-type phantom that can adapt to the MNG to enhance its usability and obtain accurate and stable results.

Manuscript received 15 March 2023; revised 6 May 2023; accepted 17 May 2023. Date of publication 22 May 2023; date of current version 24 October 2023. Corresponding author: Y. Adachi (e-mail: adachi@ael.kanazawa-it.ac.jp).

Color versions of one or more figures in this article are available at https://doi.org/10.1109/TMAG.2023.3278745.

Digital Object Identifier 10.1109/TMAG.2023.3278745

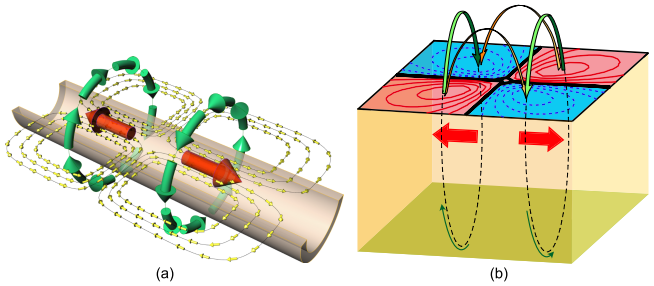

Fig. 1. (a) Schematic of intra-axonal currents (red arrows), volume currents (yellow arrows flowing in-between the two red arrows and flowing out of the nerve), and magnetic fields (green arrows) resulting from intra-axonal currents (magnetic fields generated by volume currents are not illustrated here). This figure was excerpted from [2] under CC-BY 4.0. (b) Quadrupole-like pattern of magnetic field distribution observed over the body surface. Red solid and blue dashed contour lines represent outward and inward magnetic fields, respectively. Orange arrows represent magnetic fields generated by volume current.

II. Methods

A. Design of Dry-Type Phantom for MNG

In the case of MNG/MSG, the source of the magnetic field is the local current distribution near the neural signals propagating along the axon, as shown in Fig. 1(a). The local current distribution comprises an intracellular axonal current, which is modeled using two ECDs oriented in opposite directions to each other, and an extracellular volume current compensating for the axonal current. Consequently, the magnetic field distribution observed over the body surface typically shows a quadrupole-like pattern, as shown in Fig. 1(b). The magnetic field component is in parallel to the axon originating from the volume current.

The dry-type MNG phantom was designed to realize the magnetic field distribution of the quadrupole-like pattern based on Sarvas's half-infinite planar conductor model, while the dry-type MEG phantom was based on the Sarvas's spherical conductor model. When the radius of the spherical conductor is extended to infinity, the model can be regarded as an infinite planar conductor in the half-space. Therefore, if the height of an isosceles triangular coil of the dry-type MEG phantom is extended to infinity, it can emulate the magnetic field distribution generated from the ECD of Sarvas's half-infinite planar conductor model. In this case, the moment of ECD q corresponds to the product of the short edge length d and intensity of the applied current I, that is, $q = dI$.

In practice, we chose a long rectangular coil to emulate the magnetic fields from an ECD because it was impossible to realize the isosceles triangular coil with an infinite height. To determine the size of the actual rectangular coil, a preliminary numerical experiment was performed. The length of the long edge was varied from 0.1 to 1 m, while the length of the short edge was set to 1, 3, 5, and 10 mm. The virtual observation area was assumed, in which the flux sensors were to be arranged in 180 × 160 mm area at 5 mm intervals along the XY-plane. The long rectangular coil was placed vertically at 20 mm from the center of the observation area in the Z-direction, supposing it as the shallowest magnetic source in the body. Three orthogonal components of the magnetic field at each flux sensor generated by the rectangular coils ($\boldsymbol{B}_{\text{rect}} = (B_{\text{rect},1x}, B_{\text{rect},2x}, \ldots, B_{\text{rect},1y}, B_{\text{rect},2y}, \ldots, B_{\text{rect},1z}, B_{\text{rect},2z}, \ldots)$) were calculated and evaluated in comparison

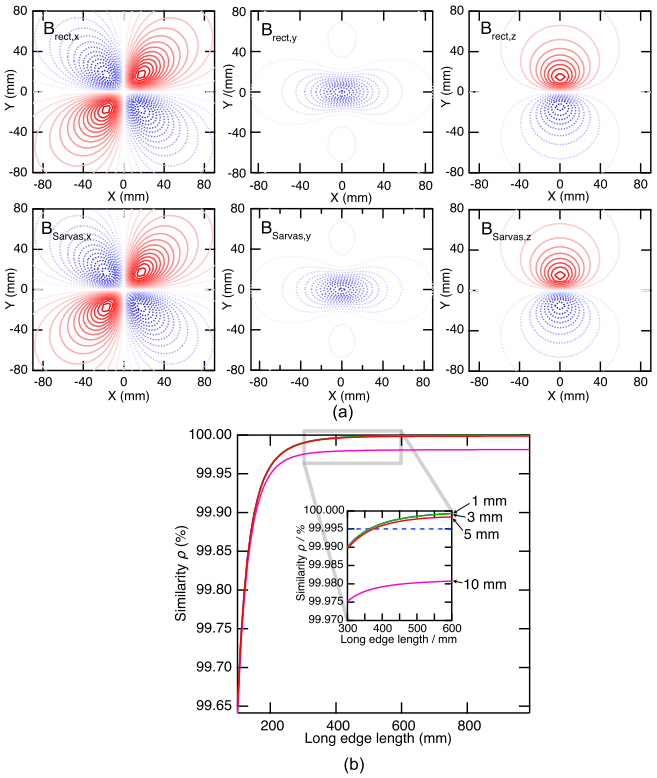

Fig. 2. (a) Example of comparison of magnetic field distribution calculated from rectangular coil and Sarvas's ECD (the short and long edges of the coil correspond to 5 and 400 mm, respectively). Red solid and blue dotted contour lines represent positive and negative directions, respectively. (b) Similarity between magnetic field distribution calculated from rectangular coil, $\boldsymbol{B}_{\text{rect}}$, and Sarvas's ECD, $\boldsymbol{B}_{\text{Sarvas}}$.

with the ones obtained from Sarvas's equation ($\boldsymbol{B}_{\text{Sarvas}} = (B_{\text{Sarvas},1x}, B_{\text{Sarvas},2x}, \ldots, B_{\text{Sarvas},1y}, B_{\text{Sarvas},2y}, \ldots, B_{\text{Sarvas},1z}, B_{\text{Sarvas},2z}, \ldots)$) described in the Appendix. The similarity ρ between the two magnetic field distributions, $\boldsymbol{B}_{\text{rect}}$ and $\boldsymbol{B}_{\text{Sarvas}}$, was calculated as

$$\rho = \left(1 - \frac{|\boldsymbol{B}_{\text{Sarvas}} - \boldsymbol{B}_{\text{rect}}|^2}{|\boldsymbol{B}_{\text{Sarvas}}|^2}\right) \times 100. \tag{1}$$

Fig. 2 shows the results of the numerical experiment when both, an ECD and a short edge of the rectangular coil, were assumed to be positioned at $(X, Y) = (0, 0)$ and oriented along the x-axis. Both the magnetic field distributions were considerably similar to each other. As shown in Fig. 2(b), the longer length of the long edge leads a higher similarity.

Considering the accuracy and easy manufacturing, the coils were fabricated by patterning on a printed circuit board (PCB). The length of the long edge of the rectangular coil was fixed at 360 mm owing to the limited availability of PCB sizes. When the long edge is 360 mm, the length of the short edge, shorter than 5 mm, provides a similarity of more than 99.994%, as shown in Fig. 2(b). Therefore, the size of the long rectangular coil was determined as 5 × 360 mm. Two of the coils with five turns were patterned in parallel on a PCB to realize the two ECDs oriented in opposite directions to each other and emulated the quadrupole-like pattern of the magnetic field distribution. The tolerance of the patterning on the PCB was 0.1 mm, and the distance between the two coils was set to 40 mm, similar to the wet-type phantom proposed

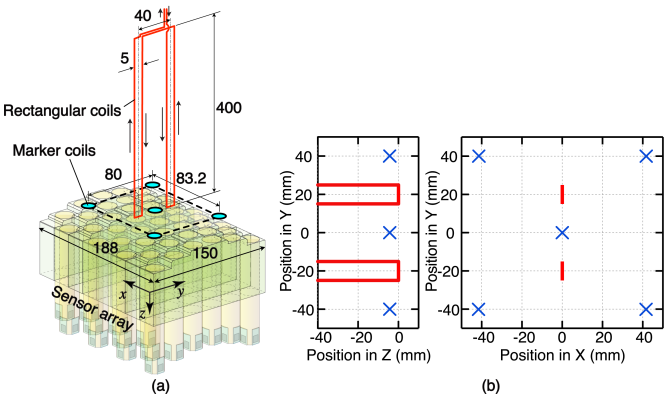

Fig. 3. (a) Experimental setup for the measurement of magnetic field using dry-type MNG phantom. (b) Positions of marker coils (blue crosses) and rectangular coils (red lines) in phantom coordination system.

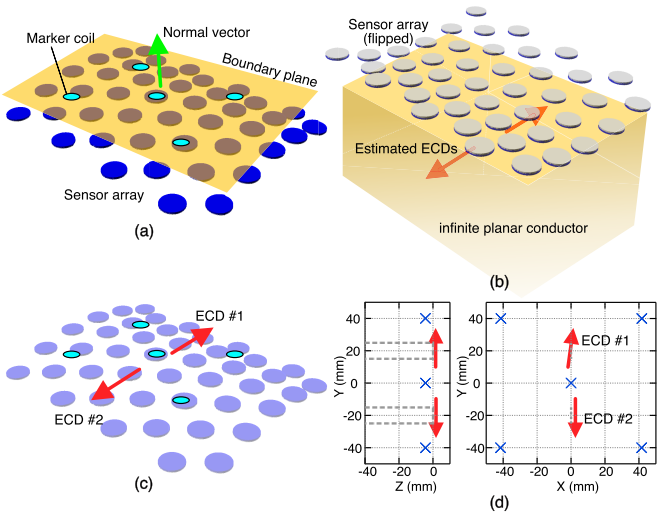

Fig. 4. Procedure for magnetic source analysis of dry-type MNG phantom with two rectangular coils. (a) Determination of boundary plane and its normal vector. (b) ECD estimation in the rotated coordinate system. (c) Inverse transform back to the sensor array coordination system. (d) Transformation to phantom coordination system and evaluation of deviation.

in our previous study [13], so that the results from both the phantoms could be compared.

B. Measurement of Magnetic Fields Using Dry-Type MNG Phantom

We demonstrate the evaluation of the MNG system using the proposed dry-type MNG phantom. Two ECDs were assumed as the source model to form the quadrupole-like pattern. The experimental setup is illustrated in Fig. 3. The dry-type phantom was composed of two rectangular coils connected in series. A sinusoidal 80 Hz burst current of intensity 0.08 mA was applied to both coils in opposite directions to each other. The duration was set to 300 ms corresponding to 24 periods. The phantom was positioned on the observation area of the 132-ch MNG system installed at Tokyo Medical and Dental University [1]. The magnetic field distribution from the coils was captured through its sensor array, which was composed of vector-type SQUID gradiometers arranged in an area of 188 × 150 mm, so that they could detect the three orthogonal components of the magnetic field simultaneously. The sensor array was calibrated after cooling using multiple circular coil arrays [15]. Five marker coils were fixed at specific relative positions around the phantom, as shown in Fig. 3(b).

The magnetic fields from the phantom were digitally recorded at the sampling rate of 1 kHz after applying the band-pass filter of 5–300 Hz. More than 60 bursts were obtained during the 2 min recording, and they were averaged to improve the signal-to-noise ratio. Using this setup, the displacement between the positions of the assumed and estimated ECDs was evaluated through the magnetic source analysis.

To clarify the deviation of the magnetic source analysis, the magnetic field distribution was acquired 40 times as the phantom location was varied randomly near the center of the sensor array. Each time the phantom location was changed, the marker coil localization was examined to determine the position and orientation of the phantom relative to the sensor array.

C. Evaluation of Magnetic Source Localization Using the Phantom

Magnetic source analysis was applied to the obtained magnetic field distribution from the dry-type MNG phantom. The position, orientation, and current intensity of the short edges of each rectangular coil were estimated as the parameters of the two ECDs based on Sarvas's half-infinite planar conductor model, and the estimated values were compared to their assumed values. The magnetic source analysis was performed for each of the 40 trials according to the following procedure.

1) The 80 Hz component was extracted from each obtained magnetic signal using the fast Fourier transform to refine the magnetic field distribution from the dry-type MNG phantom.
2) To apply (A.1), given in the Appendix, to solve the forward problem and obtain the theoretical magnetic fields, the boundary plane of the half-infinite planar conductor has to be defined. A plane including the estimated positions of the five marker coils was determined using the least squares method, and the unit normal vector of the plane was obtained. This unit vector indicates the orientation of the long edge of the rectangular coils, and the determined plane corresponds to the boundary plane [Fig. 4(a)].
3) To transform the normal vector of the plane to the unit vector along the z-axis, the rotation matrix $\mathbf{R}$ was obtained. The position and orientation of all the sensors were transformed in accordance with the obtained $\mathbf{R}$. Through this rotation, the boundary plane was transformed to the XY-plane.
4) The position, orientation, and moment of the two ECDs were estimated independently by solving the inverse problem based on the measured magnetic signals $\boldsymbol{B}_{\mathrm{meas}}$ and transformed sensor positions. The Nelder–Mead method with basin hopping optimization provided by the SciPy library [16] was applied to search the optimal ECD parameters numerically to minimize the evaluation function E, which is defined as

$$E = |\boldsymbol{B}_{\mathrm{cal}} - \boldsymbol{B}_{\mathrm{meas}}|^2. \tag{2}$$

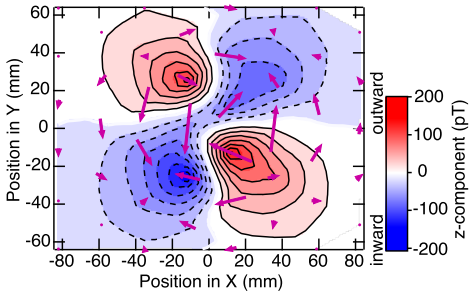

Fig. 5. Example of captured magnetic field distribution from the dry-type MNG phantom positioned at the center of the observation area. In the contour map, solid and dotted lines represent the outward and inward directions in the z-component, respectively. Purple arrows represent the tangential components.

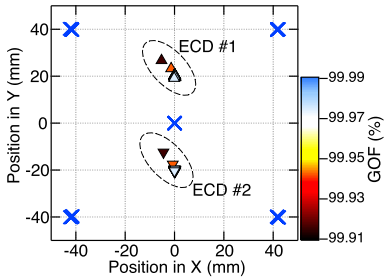

Fig. 6. Estimated ECD positions from each of the 40 trials with regard to the phantom coordination system. Blue crosses and filled triangles represent the positions of marker coils and ECDs, respectively. The color of the triangles indicates the GOF of numerical search.

Theoretical magnetic field $\boldsymbol{B}_{\text{cal}}$ was calculated as a linear summation of the magnetic fields from the two ECDs using (A.1) [Fig. 4(b)]. The number of basin hopping iterations, temperature parameter, and maximum step size were set to 50, 1.0, and 0.0001, respectively.

5) The obtained ECDs were inversely transformed using $\mathbf{R}^{-1}$. This transforms the parameters of each ECD to those described in the sensor array coordination system [Fig. 4(c)].
6) To clarify the deviation of the estimated ECD parameters from their assumed values, rigid body transformation [17] was applied to the estimated ECD parameters described in the sensor array coordination system to those in the phantom coordination system shown in Fig. 3(b) based on the positions of the marker coils [Fig. 4(d)].

III. Results

Fig. 5 shows an example of the magnetic field distribution obtained from the dry-type MNG phantom positioned at the center of the observation area oriented along the y-axis. The contour and arrow maps represent the normal and tangential components, respectively. The maximum intensity of the obtained magnetic field corresponds to 180 pT.

Fig. 6 shows the positions of the estimated ECDs from each of the 40 trials with regard to the phantom coordination system, which corresponds to Fig. 4(d). The color of each triangle corresponds to the goodness of fit (GOF) in numerical search represented by

$$\text{GOF} = \left(1 - \frac{|\boldsymbol{B}_{\text{cal}} - \boldsymbol{B}_{\text{meas}}|^2}{|\boldsymbol{B}_{\text{meas}}|^2}\right) \times 100. \tag{3}$$

TABLE I
Displacements of Estimated ECDs

	ΔX (mm)	ΔY (mm)	ΔZ (mm)	$\Delta\theta_{xy}$(deg)
ECD #1	−0.12 ± 0.14	0.31 ± 0.19	0.12 ± 0.05	−0.04 ± 0.05
ECD #2	−0.09 ± 0.12	0.15 ± 0.21	0.12 ± 0.05	−0.08 ± 0.05

Values following the signs correspond to the standard errors calculated from the 40 trials.

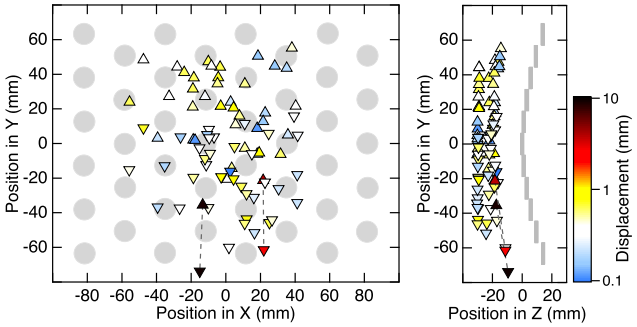

Fig. 7. Positions of estimated ECDs plotted in the sensor array coordination system. Filled gray circles represent the position of the flux sensors. Left and right plots correspond to top and lateral views of sensor array, respectively. "Upward" and "downward" triangles represent ECD #1 and ECD #2, respectively. Color of the triangles indicates displacement between assumed and estimated positions of ECDs. Triangles connected by dashed lines represent the trials with displacements larger than 1 mm.

The average and standard deviation of the GOF were 99.97 ± 0.02%. Except for two trials, the displacements between the assumed and estimated ECDs were less than 1 mm. Averaged displacements with standard errors are listed in Table I. The displacement in orientation is represented by the angle from the y-axis projected on the XY-plane ($\Delta\theta_{xy}$) because the z-component of the ECD moment estimated by the magnetic source analysis based on Sarvas's half-infinite planar conductor model is indefinite.

Fig. 7 shows the positions of the ECDs transformed to the sensor array coordination system, which corresponds to Fig. 4(c). The color of each triangle represents the displacements in the position calculated as $\Delta R = (\Delta X^2 + \Delta Y^2 + \Delta Z^2)^{0.5}$.

IV. Discussion

The quadrupole-like pattern of the magnetic field distribution, including the y-component in parallel to the short edges of the rectangular coils, was clearly observed, as shown in Fig. 5. It indicates that the magnetic fields from the volume current were emulated in addition to the other components in accordance with the theory.

The averaged displacement values shown in Table I are reasonable considering the patterning tolerance of the PCB. Regarding the two trials with the large displacements, the GOFs of these trials were inferior to those of the other trials. However, the distance between the two dipoles, which is not shown, was in good agreement with the assumed value of 40 mm. This suggests that the ECD localization was successfully performed. As shown in Fig. 7, the phantom positions of these trials were in an inclined region at the edge of the sensor array area. Therefore, we speculate that the cause of the large displacements in these two trials was

that the phantom could not be fixed firmly and it had slightly slipped off the surface of the sensor array area before the measurement for marker coil localization. However, as this could not be confirmed, we decided not to remove these trials from the results.

Regarding the comparison to the wet-type phantom proposed in our previous study, the GOF between the theoretical and measured magnetic field distribution was calculated as $99.97 \pm 0.02\%$, as described in Section III, while the one from the wet-type phantom was $95.66 \pm 0.24\%$ [13]. Although the difference between the GOFs includes not only the difference of the phantoms but also the differences of the MNG systems and measurement conditions, it is suggested that the dry-type MNG phantom could emulate the quadrupole-like magnetic field distribution at a comparable or higher accuracy than the wet-type MNG phantom.

The frequency band of the MNG signals treated in this study is less than several kilohertz. Therefore, the quasi-static magnetic field condition was satisfied, and the effect of the dielectric properties and losses in the body tissues was negligible. However, if the frequency band of the target signal is higher than the several kilohertz, the dry-type phantom is not applicable because it cannot emulate those parameters of the body unlike the wet-type phantom.

In this study, the current driver to excite the rectangular coils was a customized electric circuit and was not precisely calibrated. Therefore, the accuracy of the estimation of the moment is not discussed. An investigation of the accuracy of the estimated ECD moment using a calibrated current driver and a discussion of the magnetic source estimation at lower current values will be studied in the future.

V. Conclusion

We proposed a dry-type phantom for the evaluation of the MNG system. The phantom is composed of a PCB patterned with two long rectangular coils in parallel, with the short and long edges measuring 5 and 360 mm, respectively. Each coil generates approximately the same magnetic fields as those from the ECDs of Sarvas's planar conductor model. When current was applied to both the coils in opposite directions to each other, the phantom could emulate the quadrupole-like pattern of the magnetic field distribution typically observed in MNG. The dry-type phantom was easier to handle and provided the comparable or higher accuracy than that of the previously developed wet-type phantom in terms of GOF. It was effective in the evaluation of algorithms of the magnetic source analysis to compare the different MNG systems or different measurement conditions and to check the system performance for maintenance and for various other applications.

Appendix

The magnetic field at a certain point $\boldsymbol{B}(\boldsymbol{r})$ from an ECD of Sarvas's half-infinite planar conductor model $\boldsymbol{Q}(\boldsymbol{r}_0)$ is calculated as [12]

$$\boldsymbol{B}(\boldsymbol{r}) = \frac{\mu}{4\pi K}(\boldsymbol{Q} \times \boldsymbol{a}\cdot\boldsymbol{e}_z \nabla K - K\boldsymbol{e}_z \times \boldsymbol{Q}) \tag{A.1}$$

assuming that the planar conductor is in parallel to the XY-plane and where μ is the permeability, $\boldsymbol{a}$ is the relative position expressed as $\boldsymbol{a} = \boldsymbol{r} - \boldsymbol{r}_0$, $\boldsymbol{e}_z$ is the unit vector along the z-axis, and K and ∇K are defined as follows:

$$K = a(a + \boldsymbol{a} \cdot \boldsymbol{e}_z) \tag{A.2}$$

$$\nabla K = \left(2 + \frac{\boldsymbol{a} \cdot \boldsymbol{e}_z}{a}\right)\boldsymbol{a} + a\boldsymbol{e}_z. \tag{A.3}$$

$\boldsymbol{B}(\boldsymbol{r})$ includes the magnetic fields from both, an ECD in the half-infinite planar conductor and the volume current to compensate for the ECD. The z-component of the ECD moment does not contribute to $\boldsymbol{B}(\boldsymbol{r})$ because of the structural symmetry.

Acknowledgment

The authors would like to thank Editage for the English language editing (www.editage.jp).

References

[1] Y. Adachi et al., "Multichannel SQUID magnetoneurograph system for functional imaging of spinal cords and peripheral nerves," *IEEE Trans. Appl. Supercond.*, vol. 31, no. 5, Aug. 2021, Art. no. 1600405.

[2] S. Sumiya et al., "Magnetospinography visualizes electrophysiological activity in the cervical spinal cord," *Sci. Rep.*, vol. 7, no. 1, p. 2192, May 2017.

[3] J. Hashimoto et al., "Assessment of thoracic spinal cord electrophysiological activity through magnetoneurography," *Clin. Neurophysiol.*, vol. 133, pp. 39–47, Jan. 2022.

[4] T. Watanabe et al., "Novel functional imaging technique for the brachial plexus based on magnetoneurography," *Clin. Neurophysiol.*, vol. 130, no. 11, pp. 2114–2123, Nov. 2019.

[5] Y. Bu et al., "Peripheral nerve magnetoneurography with optically pumped magnetometers," *Frontiers Physiol.*, vol. 13, Mar. 2022, Art. no. 798376.

[6] T. Yamamoto, S. J. Williamson, L. Kaufman, C. Nicholson, and R. Llinas, "Magnetic localization of neuronal activity in the human brain," *Proc. Nat. Acad. Sci. USA*, vol. 85, pp. 8732–8736, Nov. 1988.

[7] R. M. Leahy, J. C. Mosher, M. E. Spencer, M. X. Huang, and J. D. Lewine, "A study of dipole localization accuracy for MEG and EEG using a human skull phantom," *Electroencephalogr. Clin. Neurophysiol.*, vol. 107, no. 2, pp. 159–173, Apr. 1998.

[8] D. Oyama, Y. Adachi, M. Yumoto, I. Hashimoto, and G. Uehara, "Dry phantom for magnetoencephalography—Configuration, calibration, and contribution," *J. Neurosci. Methods*, vol. 251, pp. 24–36, Aug. 2015.

[9] D. Cohen and H. Hosaka, "Magnetic field produced by a current dipole," *J. Electrocardiol.*, vol. 9, no. 4, pp. 408–417, 1976.

[10] G. Uehara et al., "An effect of electrical double layer on MEG phantom with saline water," *Int. Cong.*, vol. 1300, pp. 611–614, Jun. 2007.

[11] R. J. Ilmoniemi, M. S. Hämäläinen, and J. Knuutila, "The forward and inverse problems in the spherical model," in *Biomagnetism: Applications & Theory*. New York, NY, USA: Pergamon, 1985, pp. 272–282.

[12] J. Sarvas, "Basic mathematical and electromagnetic concepts of the biomagnetic inverse problem," *Phys. Med. Biol.*, vol. 32, no. 1, pp. 11–22, Jan. 1987.

[13] Y. Adachi, D. Oyama, S. Kawabata, M. Sato, and G. Uehara, "Realistic neural current model for developing a phantom for the evaluation of spinal cord biomagnetic measurement," *IEEE Trans. Magn.*, vol. 47, no. 10, pp. 3837–3840, Oct. 2011.

[14] Y. Adachi, D. Oyama, N. Somchai, S. Kawabata, and G. Uehara, "Simplified spinal cord phantom for evaluation of SQUID magnetospinography," *J. Phys., Conf.*, vol. 507, no. 4, May 2014, Art. no. 042001.

[15] Y. Adachi, M. Higuchi, D. Oyama, Y. Haruta, S. Kawabata, and G. Uehara, "Calibration for a multichannel magnetic sensor array of a magnetospinography system," *IEEE Trans. Magn.*, vol. 50, no. 11, Nov. 2014, Art. no. 5001304.

[16] *SciPy v1.10.1 Manual*. Accessed: Feb. 19, 2023. [Online]. Available: https://docs.scipy.org/doc/scipy/reference/generated/scipy.optimize.basinhopping.html

[17] J. H. Challis, "A procedure for determining rigid body transformation parameters," *J. Biomechanics*, vol. 28, no. 6, pp. 733–737, Jun. 1995.